Version of Record: https://www.sciencedirect.com/science/article/pii/S1369702121002030
Manuscript_3a71abc2da9dcf98354bc23757bca713

The effects of static local distortions vs. dynamic thermal motions on the stability and band gaps of cubic oxide and halide perovskites

Xin-Gang Zhao[1], Zhi Wang[1], Oleksandr I. Malyi[1] and Alex Zunger[1,*]

1. Renewable and Sustainable Energy Institute, University of Colorado, Boulder, Colorado 80309

Ternary ABX_3 perovskites made of corner-sharing BX_6 octahedra have long featured prominently in solid-state chemistry and condensed matter physics. Still, the joint understanding of their two main subgroups—*halides and oxides*– has not been fully developed. Indeed, unlike the case in simpler compounds having a single, robust repeated bonding motif ("monomorphous"), certain cubic perovskite can manifest a non-thermal (=intrinsic) distribution of local motifs ("polymorphous networks"). Such static deformations can include positional degrees of freedom (e.g., displacements and tilting) or magnetic moment degrees of freedom (in paramagnets made of oxide perovskites with B atoms containing *d* orbitals). Unlike thermal motion, such static distortions do not time-average to zero, being an expression of the intrinsic symmetry breaking preference of the chemical bonding. The present study compares electronic structure features of oxide and halide perovskites starting from the static polymorphous distribution of motifs described by DFT minimization of the internal energy, continuing to finite temperature thermal disorder modeled via finite temperature DFT Molecular dynamics. We find that (i) Different *oxides vs. halide* ABX_3 compounds adopt different energy lowering symmetry-breaking modes. The calculated pair distribution function (PDF) of $SrTiO_3$ from the first-principles agrees with recently measured PDF; (ii) In both oxides and halides, such static distortions lead to band gap *blueshifts* with respect to undistorted cubic Pm-3m structure (iii) For ABO_3 perovskites, high-temperature molecular dynamics simulations initiated from the statically distortion polymorphous structures reveal that *thermally-induced* distortions can lead to a band gap *redshift*. (iv) In contrast, for cubic *halide* perovskite $CsPbI_3$, both the intrinsic distortions and the thermal distortions contribute in tandem to band gap *blueshift*, the former, intrinsic effect being dominant. (v) In the oxide $SrTiO_3$ and $CaTiO_3$, (but not in halide) perovskites octahedral tilting leads to the emergence of a distinct Γ-Γ direct band gap component as a secondary valley minimum to the well-known indirect R-Γ gap. Understanding such intrinsic vs. thermal effects on oxide vs. halide perovskites holds the potential for designing target electronic properties.

Keywords: Perovskites, symmetry breaking, band gap renormalization, Pair Distribution function, polymorphous networks; $SrTiO_3$, $CaTiO_3$, $CsPbI_3$

© 2021 published by Elsevier. This manuscript is made available under the Elsevier user license
https://www.elsevier.com/open-access/userlicense/1.0/

I. Introduction

ABX_3 halides perovskites $A^{(I)}B^{(IV)}X_3^{(VII)}$ and oxides Perovskites $ABO_3^{(VI)}$ often crystalize as corner-sharing low-symmetry (e.g., orthorhombic or tetragonal) perovskite phases at low temperatures (LT), sometimes transforming at higher temperatures into the cubic perovskite phase. They are generally discussed in terms of the nature of the microscopic degree of freedom, be that the magnetic moments (in ferromagnet/paramagnet), or electric dipoles (in ferroelectric/paraelectric), or octahedral degrees of freedom (e.g., tilting and rotations).[1–5] X-ray diffraction (XRD) measurements[6] on such cubic perovskites have traditionally been modeled by the nominal cubic Pm-3m space group structure containing a single ABO_3 formula unit, with undistorted octahedra, where atoms reside on the nominal Wyckoff positions.[7]

Such single-motif (*monomorphous*) cubic (Pm-3m) models of numerous oxide and halide perovskites[8–10] have been extensively used over years in the theoretical literatures as input to the electronic band structure, [11–19] and phonon lattice dynamics, [20–26] constituting the basis for the currently accepted interpretation of a broad range of electronic properties.[27–38]

However, theoretical predictions of electronic and structural properties based on such nominal cubic models do not always agree with experimental observations on the corresponding pristine bulk compounds. Puzzling contradictions include the observation of effects commonly known to be enabled by non-cubic symmetry, yet seen in nominally cubic phases, such as piezoelectricity in paraelectric $BaTiO_3$,[33] Rashba effect in $CsPbCl_3$,[34] and second harmonic generation (SHG) in $BaTiO_3$.[35] Furthermore, cubic models for phonon dispersion calculations often predicted dynamically unstable phonons in $BaOsO_3$, $SrMnO_3$, and $SrFeO_3$.[36,37] In addition to these qualitative failures, *quantitative* disagreements were noticed between electronic structure calculations based on the nominal cubic structure and measurements, such as the predicted absence of effective mass enhancement in $SrVO_3$, $BaTiO_3$, $LaMnO_3$, and $SrBiO_3$,[29] underestimated band gaps not only for halide perovskite insulators such as $CsSnI_3$ $CsPbI_3$ and $CsPbBr_3$,[28,38] but more dramatically, the prediction of metallic electronic structures for known (Mott) insulators such as $CaMnO_3$, $LaFeO_3$, $LaVO_3$, $YNiO_3$ $LaTiO_3$, and $YTiO_3$.[30–32]

***The views of two communities on the nature of the para-phases*:** Two leading communities—the 'phase transition community' and the 'electronic structure community'—are grappled with the understanding of the phase transition between the long-range ordered (LRO) low-temperature phases (e.g., orthorhombic, monoclinic, and tetragonal) and the high-temperature para-phases that lack LRO.

The '***phase transition community***' focused initially on two pictures: **(1A)** The ***displacive/soft-mode picture*** emphasizing time averaging, thermal displacements, and reciprocal space treatments of phonons,

based on the monomorphous, high-symmetric minimal cell such as the cubic (Pm-3m) structure. A key feature of assuming a monomorphous structure is that all *static distortions* are thought to be negligible, and atoms are oscillating thermally around their Wyckoff positions. Therefore, one can always apply the *time-average* to the observable properties. *Reciprocal-space* calculation of phonons is applied, often leading to the softening of the specific optic phonon (such as the F_{1u} mode) as the transition to the lower-temperature low-symmetry phase is approached, where this mode is replaced by the lower symmetry modes of the LT phase. The displacive model was supported by early theoretical studies[39–41] that predicted no atomic displacement in the high-symmetry phases and no phase transition until strains were induced.

However, it was later realized experimentally that some crystals show static symmetry breaking in the high-symmetry para-phases. This approach is known as the **(1B) *order-disorder picture***, which emphasizes spatial averaging, static displacements, and a real-space treatment of the ordering process. Examples include the multi-site off-center displacement model[33,40–43] in ferroelectric perovskites. The phonon modes obtained in such systems could include modes that do not soften, such as the "central mode" representing jumps between potential wells. In contrast, in the displacive view, the system oscillates in a single well creating a soft mode.[44]

The '***electronic structure community'*** grappled with the question of how to represent the microscopic atomic-scale structure of the para-phase needed for both phonon and band structure calculations. The properties of interest were not restricted to phonon, but included optical properties, transport (e.g., metal vs. insulator), etc. Early approximations involved using a monomorphous model, representing the *average* atomic structure (e.g., a non-electric representation of a paraelectric phase) or *average* spin structure (e.g., a non-magnetic representation of a paramagnet). Such monomorphous descriptions of the para-phases end up in electronic structure calculations with an artificially high symmetry (virtual-crystal-like), i.e., centrosymmetric (here, Pm-3m) structure. Such calculations for cubic oxide[45,46] and cubic halide[38] perovskites have been shown to give significant contradictions with the experiment. For *d*-electron paramagnets such as $LaTiO_3$,[47,48] a monomorphous model resulted in the metallic band structure, even though they are known to be (Mott) insulators. In cubic halides, the predicted band gap values were anomalously underestimated. Such broad disagreements between experiments and calculations based on the monomorphous approach were generally addressed in the '*electronic structure community'* by two diverging approaches: In approach **2A (dynamic correlation in symmetry unbroken structures),** the use of simple periodic monomorphous cell persisted. In the cases of *oxide perovskites*, the predicted false metallic states in *d*-electron cubic perovskites[31,32] and the absence of mass

enhancement[29] motivated, in part, the development of the "theory of strongly correlated compounds".[49] In such approaches, the nominal high-symmetry monomorphous structures were retained. But strong interelectronic correlations codified by the Mott-Hubbard electron repulsion *U* were invoked in the symmetry unbroken (monomorphous) structures to reconcile such predicted electronic discrepancies with measurements. This was addressed by introducing *time fluctuation* in the microscopic dipole, magnetic moments, geometric tilting, which could lead to an average zero polarization (in the paraelectric phase), or an average zero magnetic moment (in the paramagnetic phase). The second approach **(2B) is mean field theory in symmetry broken structures**, such as Density Functional Theory. Initially, in this approach, the disorder in the para phases was treated by 'structural approximants' avoiding molecular dynamics. Notable examples include the "Virtual Crystal Approximation" (VCA),[50] or "Coherent Potential Approximation" (CPA),[51]. These approaches offer an effective configuration that could be used as input to standard electronic structure theory and capture some aspects of disorder. Whereas such models are ubiquitous for *positionally disordered alloys*, they are not generally applicable for crystallographically ordered single-phase compounds. The discrepancies above between such simple monomorphous models and experiments are therefore a persistent difficulty. Approach (2B) then abandoned the simple VCA and CPA and further abandoned the monomorphous restriction by using instead supercell that affords spatial symmetry breaking. It was pointed out that static symmetry-breaking can occur spontaneously if no artificial (e.g., monomorphous) restrictions were placed. This leads to the emergence of distribution of local motifs in the form of a distribution of non-zero magnetic moments (in paramagnets), or electric dipoles (in para electrics) or atomic displacements (in para elastic), or a mixture of such microscopic degrees of freedoms.[27–30] Furthermore, such a formation of a *polymorphous network* is accompanied by a lowering of the internal energy. [The term *polymorphous network* refers to different local motifs (i.e., presenting microscopically different DOWPs in different local environments) in the *same phase* instead of different local motifs in different phases. The latter is known as polymorphs].

This paper will address the difficulties mentioned above in oxide and halide cubic perovskites by investigating the different local *environments both statically and via thermal effect, replacing at the outset the monomorphous approach by the polymorphous extension*. The starting point of this discussion is that the tradition of seeking the smallest possible, highest symmetry unit cell is not protected by fundamental physical principles, and may need to be relaxed under some circumstances. Indeed, the real cubic perovskite phase may manifest a distribution of positional degrees of freedom (e.g., displacements and tilting[52]), or magnetic moment degrees of freedom (as in paramagnets[53]), or local dipole degrees of freedom (as in paraelectrics[33]) even in single phase compounds. It was pointed out[27–30] that unlike

the case in simpler compounds having intrinsically a single, robust repeated bonding motif (e.g., the tetrahedron in covalent semiconductors), the chemical bonding in certain cubic perovskite create a static distribution of energy lowering local motifs referred to as a polymorphous network[28,29]. The deriving forces for stabilizing such symmetry-breaking are varied, and can include lone pair electrons (in B^{2+} = Pb, Sn, etc.), or Jahn-Teller ions, leading to static atomic Distortions off Wyckoff Position (hereafter, DOWPs). Such polymorphous networks manifest a lower calculated internal energy U_0 of the non-vibrating lattice relative to the monomorphous network. This energy lowering associated with the formation of static DOWPs can be evaluated by constraining the global shape of the structure to the cubic symmetry and minimizing the internal energy with respect to all cell-internal (atomic positions, e.g., octahedral tilting and ferroelectric displacement) degrees of freedom.[25,26,28] Such static DOWPs do not time-average to zero, as thermal motions do, being an expression of the intrinsic symmetry breaking preference of the chemical bonding.

II. The type of systems discussed in the current symmetry broken polymorphous approach: Static and dynamic

We will discuss two types of distortions: First, *single-mode* distortions are isolated DOWPs such as single Glazer mode, B site off-center, Jahn-Teller distortion and breathing modes. These single-mode distortions are explored in 2x2x2 supercell by freezing in a particular distortion mode, one at the time of a given amplitude, keeping the structure frozen. This is done for the general understanding of how specific compounds respond to given symmetries of single DOWPs. Second, our primary calculation of ***polymorphous structure*** involves allowing for *multi-mode in a* cubically shaped 4x4x4 supercell, where all atoms are relaxed by nudging their positions and following the Hellman-Feynman forces.

Table I provides an overview of the general trends in DFT results of how static multi-mode and dynamic distortions affect different properties such as band gaps in two prototype cubic perovskites, $SrTiO_3$ and $CaTiO_3$. The reason for choosing these systems is that we plan to study the effects on stabilities and band gap values due to the distortions related to different Goldschmidt factor and band-edge states. (In this paper, we mainly focus on the semiconductors oxide ABO_3 (A=Ba, Sr, Ca, Pb; B=Ti, Zr), $SnTaO_3$ and halide $CsBX_3$ (B=Ge, Sn, Pb; X=F, Br, I), $KPbI_3$ and $RbPbI_3$). shows three structural depictions of the cubic phases: (a) the highly symmetric nominal cubic (Pm-3m) structure that prohibits distortions, as well as the (b) static, non-thermal multi-mode distortions characteristic of the polymorphous network obtained through T=0 energy minimization of DFT cubic supercell and (c) the structure obtained at finite temperature from DFT molecular dynamics. The main features we wish to discuss are:

Table I. Overview of Density functional theory results discussed in the present paper of atomic distortions and ensuing calculated band gaps in three renderings of the cubic perovskite structure for $SrTiO_3$ and $CaTiO_3$: (a) nominal cubic Pm-3m model disallowing atomic distortions results in lower band gap energies; (b) Supercell model allowing intrinsic, static, energy lowering multi-mode distortions *raises* the band gap, and (c) Dynamic thermal motion captured by molecular dynamics *reduces* the band gap at sufficiently high temperatures limit (5x5x5 $SrTiO_3$ supercell at 1400 K;[54] 4x4x4 $CaTiO_3$ supercell at 2000 K).

Compounds	**Property**	**Configurations of cubic $SrTiO_3$ and $CaTiO_3$**		
		(a)	**(b)**	**(c)**
		No distortion	**Static distortion**	**Thermal distortion**
$SrTiO_3$	Sr displacements (Å)	0.00	0.02-0.04	0.00-0.72
	Ti displacements (Å)	0.00	0.06-0.08	0.00-0.57
	O_6 tilting angle (°)	0.00	0-7	0-19
	Band gap (eV)	1.63	1.86	1.14
$CaTiO_3$	Ca displacements (Å)	0.00	0.00-0.08	0.01-0.80
	Ti displacements (Å)	0.00	0.01-0.12	0.01-0.77
	O_6 tilting angle (°)	0.00	1-15	0-26
	Band gap (eV)	1.70	2.08	0.93

(1) Static multi-mode distortions led to energy lowering symmetry breaking generally associated with blue shifts in the band gaps: The (a) nominal monomorphous cubic structure excludes by symmetry possible DOWPs, leading in electronic band structure calculations to underestimated band gaps. At the extreme, in oxides with d electron B atoms, monomorphous models of paramagnets lead to false metallic states.[55] (b) Intrinsic *static* distortions allowed in larger cubic supercells result in *band gap blueshift* in polymorphous cubic oxide perovskites $ATiO_3$ (A=Ba, Sr, Ca). We mention in passing that in Mott oxides with *d* electron B atoms, the formation of a distribution of local moments in the paramagnetic cubic phase was recently shown[28] to correctly convert false metals in the monomorphous nominal cubic case to insulators with effective mass enhancement effect,[29] in the polymorphous cubic phase, without invoking dynamic correlation effects. These effects of static DOWPs can be measured using techniques sensitive to the *local* structure, such as atomic pair distribution function (PDF) analysis and X-ray absorption fine structure (XAFS).[56,57] The polymorphous nature in cubic $SrTiO_3$ is consistent with the agreement found here between our DFT calculated pair distribution function based on polymorphous $SrTiO_3$ and experimental measurement. For halide perovskites such as $CsPbI_3$, the polymorphous network

corrects the quantitative underestimation of the calculated band gap relative to the experiment.[38] Band unfolding of the (supercell) band structure of $SrTiO_3$ and $CaTiO_3$ reveals that the energy lowering symmetry breaking results in the emergence of a direct band gap Γ-Γ component in addition to the indirect R-to-Γ transition.

(2) Dynamic distortions akin to stochastic thermal motion can lead to redshifts in the band gaps: The static DOWPs can be viewed as the low-temperature kernel of the thermal displacements associated with the non-vibrating free energy $F = U_0 - TS$. The main differences between static DOWPs and dynamic thermal distortions are that, unlike the thermal displacements whose time averages represent the equilibrium structure with atoms on the nominal Wyckoff positions, the static DOWPs do not time average into the ideal Wyckoff positions. Large amplitude static distortions in cubic oxide perovskites (octahedral tilting angle > 8°) were found to *turn over the band gap blueshift to a redshift*. Indeed, the enhanced distortions seen in our molecular dynamics simulations at high temperatures for *oxides* result in a significant band gap redshift (0.5 - 0.8 eV) in cubic $CaTiO_3$ and $SrTiO_3$ (Table I). The thermal motion could eventually decrease the band gap at high temperatures towards the limit of metallization, as is the case in $BiFeO_3$.[58] In contrast, for cubic *halide* perovskite $CsPbI_3$, the intrinsic static distortions in the polymorphous network already give a large blueshift, and the thermal effects add another (small) blueshift. This corresponds to an anomalously low thermal gap renormalization, whereas using the monomorphous reference points predicts a spuriously large thermal blue shift.[38]

III. The choice of supercell symmetry matters

The physically meaningful cell used to express diffraction data might be larger than a macroscopically averaged minimal cell. As Fig. 1 illustrates, *odd-index* replicas of the cubic (Pm-3m) cell do not allow octahedral single-mode rotation. For example, all the octahedral rotation modes denoted by the simple-mode Glazer notation[52] such as $a^0a^0b^-$, require a cell size of at least 2×2×2 or $\sqrt{2} \times \sqrt{2} \times 2$. The multi-modes DOWPs formed by more complex Glazer modes[52] are denoted, for example, as $(a^0a^0b^1)_1^2(a^0a^0b^+)_2^3(a^0a^0b^-)_3^4$ where subscript and superscript integer indices denote the $SrTiO_3$ layers along [001] direction, i.e., the first and the second ABO_3 layers along [001] direction have $a^0a^0b^-$ mode, while the second and the third layers have $a^0a^0b^+$ mode). Such modes can be represented by cell sizes of at least 2×2×4 or $2\sqrt{2} \times 2\sqrt{2} \times 4$. Importantly, none of those mentioned above rotation modes can be realized along an odd-size axis, meaning that all possible static DOWPs related to octahedral rotation will be missed in the odd-size cell such as 3×3×3 or 5×5×5. Thus, any physical effect related to *intrinsic non-*

thermal octahedral rotation DOWPs would be missed in a 5×5×5 representation used, e.g., in molecular dynamics simulations.[54]

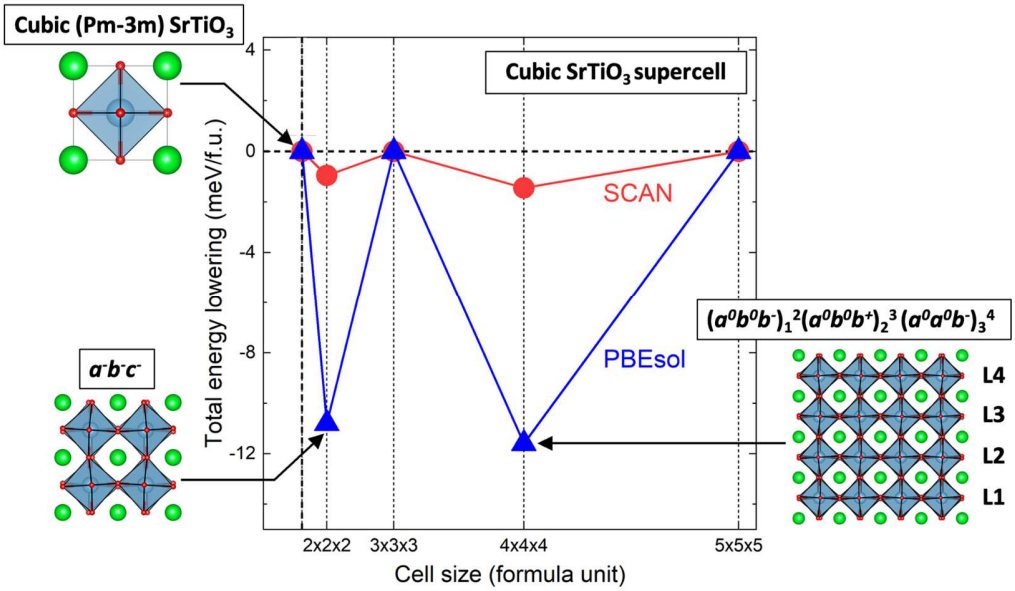

Figure 1. DFT static internal energies of the minimal cell and enlarged 2×2×2, 3×3×3, 4×4×4, and 5×5×5 supercells of cubic $SrTiO_3$ at equilibrium lattice constant. The static energy from the *minimal* cell has been chosen as the reference. Static rotation DOWPs are symmetry-forbidden in the odd-size supercells. Therefore, the minimal 1x1x1 cell, as well as 3×3×3 and 5×5×5 supercells, all show no rotation DOWPs and unchanged energy. The 2×2×2 supercell shows energy lowering due to an $a^-b^-c^-$ (Glazer notation) octahedral rotation, while the 4×4×4 supercell shows further energy lowering due to$(a^0a^0b^1)_1^2(a^0a^0b^+)_2^3(a^0a^0b^-)_3^4$ multi-mode rotation. Different DFT exchange-correlation functionals give different static energy lowering (SCAN[59] in red and PBEsol[60] in blue), but consistent energy-lowering trend and rotation modes among all cells studied. The equilibrium lattice constant a_0=3.907 Å is obtained from DFT using PBEsol functional and in good agreement with the experimental value.[61]

Once identifying the allowed symmetry of supercells needs to capture certain modes (here, even number replicas *N*), one must perform supercell energy convergence tests with respect to *N within the symmetry allowed group* until the structural and electronic properties are converged. In our calculations of ***multi-mode polymorphous structures,*** the global lattice vectors of the supercells are fixed to the macroscopically observed a=b=c cubic symmetry (otherwise, unconstrained relaxation will converge to the low-temperature low-symmetry ground states). At the same time, all cell-internal atomic positions are allowed to relax following the calculated quantum mechanical forces. The force threshold on each

atom is set to less than 0.01 eV/Å. The technical parameters are described in Supplementary section A. We use the 4×4×4 supercell consisting of 64 ABO_3 formula (320 atoms) units which is symmetry-compatible with all possible DOWPs we study. Relaxation is performed by applying random nudges on each atom in the 4×4×4 supercell with nudge amplitudes randomly selected between -0.15 to 0.15 Å with 0.01 Å steps. The initial lattice constant a=b=c for the polymorphous case was taken as the value obtained by minimizing the energy vs. volume of the monomorphous case. This was subsequently allowed to relax in the polymorphous case with the energy change less than 1 meV/atom. The present approach of multi-mode polymorphous nudging creates upon relaxation a natural distribution of *locally disordered motifs.* Whereas such polymorphous structures do inherit upon relaxation some of the local distortion motifs from the low-temperature low symmetry (orthorhombic, tetragonal) corner-shared phases. Unlike the latter, these local motifs in the nudged polymorphous structures are not necessarily spatially ordered. As such, we believe that these polymorphous networks provide useful 'structural approximants' for describing the electronic structure of realistic cubic perovskites before thermal agitation sets in. The thermally induced disorder is then added at the DFT Molecular dynamics stage (Sec. V), building upon the static polymorphous starting structure.

IV. Effects of intrinsic, static DOWPs on internal energy and local structure

A. Identification of single-mode that lower the internal energy of specific compounds

Whereas static DOWPs were defined geometrically rather early, e.g., the classic works of Glazer and others,[62,63] the question of whether they actually lower the total internal energy U_0 of particular cubic compounds requires compound-dependent total energy calculations. As Fig. 2 illustrates, not all the DOWPs in cubic compounds result in energy lowering with respect to undistorted, nominal cubic (Pm-3m) structure. Not all cubic oxide ABO_3 or halide ABX_3 compounds react in a similar way to specific DOWPs displacements. Being the result of static internal energy lowering, such DOWPs represent the expression of various bonding mechanisms such as lone-pair stereochemical effects,[18,25,64,65] Jahn-Teller distortions (i.e., electronic degeneracy removal)[30], or semiclassical Jahn-Teller-like[30] effects, thus being naturally bonding-dependent.

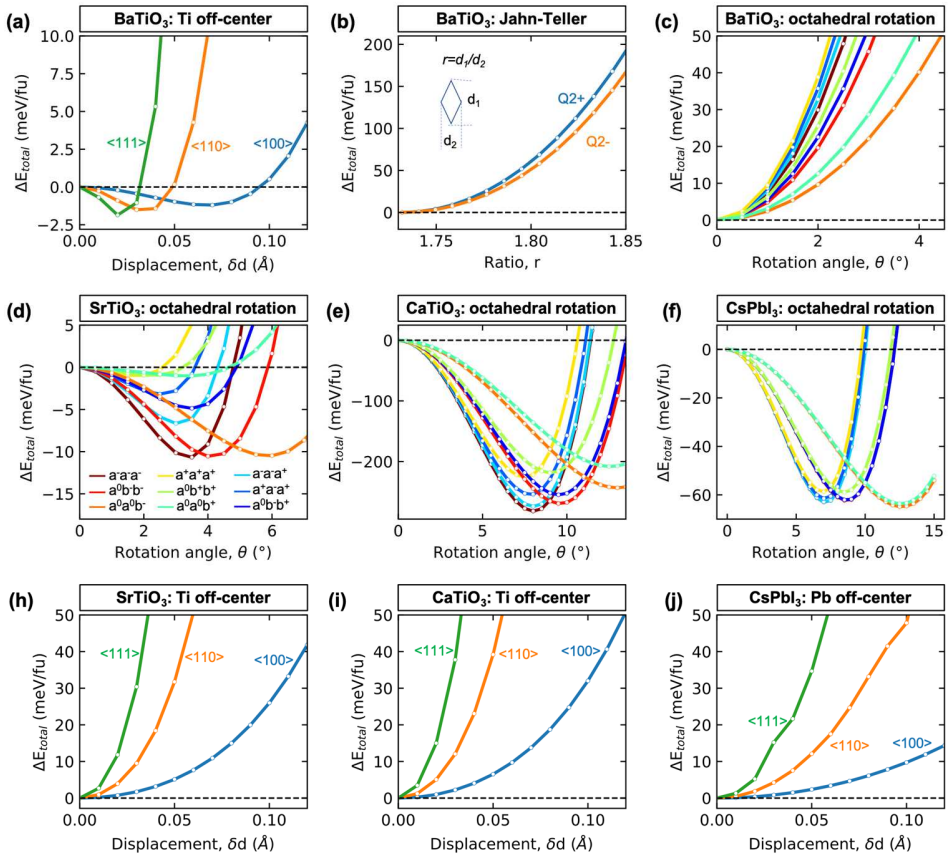

Figure 2. Illustrations of some of the symmetry-allowed single-mode distortions on static internal energy in cubic oxide and halide perovskites. All calculations use density functional theory (DFT) with PBEsol exchange-correlation functional. Single-mode is applied one at a time with frozen-in amplitude and the total energy evaluated in DFT without further relaxation. The total internal energies (y-axis) are shown where the energy zero (horizontal dash lines) is the undistorted single cubic (Pm-3m) cell. Energy changes as a function of B-site off-center displacements are shown in cubic $BaTiO_3$, $SrTiO_3$, $CaTiO_3$, and $CsPbI_3$. The frozen-in Ti off-center along [111] direction (δd=0.035 Å) results in the most significant energy lowering (1.8 meV/fu) among all the considered configurations. (b) pseudo-Jahn-Teller distortion Q_2^+, and Jahn-Teller distortion Q_2^- in cubic $BaTiO_3$; (c-f) octahedral rotation modes using the simple Glazer notation[62] in cubic $BaTiO_3$, $SrTiO_3$, $CaTiO_3$, and $CsPbI_3$. Breathing mode and lattice expansions along one, two, and three directions (defined as a, ab, abc directions) are shown in Fig. S-1 and S-2 in Supplementary section A.

Figure 2 indicates that the symmetry of single-mode energy lowering is strongly compound-dependent: for cubic $BaTiO_3$, only the Ti off-center displacement mode is energy lowering, whereas, for cubic $SrTiO_3$, $CsPbI_3$ and $CaTiO_3$, only octahedral rotation modes are energy lowering. The energy lowering

can be significant, e.g., the rotational DOWPs can lead to more than 200 meV/f.u. energy lowering relative to the undistorted structures. The corresponding rotation angles are 4° for the $a^-a^-a^-$ mode in $SrTiO_3$, 13° for the $a^0a^0b^-$ mode in $CsPbI_3$, and 8° for $a^-a^-a^-$ mode in $CaTiO_3$, as what is found in other perovskites compounds.

B. Multi-mode deformations: static internal energy lowering and the emergence of polymorphous networks

Besides the single-mode energy lowering illustrated in Fig. 2, static DOWPs can also be multi-mode (as described in section II) in polymorphous cubic $BaTiO_3$, $SrTiO_3$, $CaTiO_3$, $CsPbI_3$ and $CsSnI_3$. Such structures that have been cubically constrained and minimized in total internal energy show multi-mode, sometimes with even more considerable internal energy lowering, indicated in Table II as ΔE_M.

Table II. The DFT energy lowering ΔE_M due to multi-mode in polymorphous structures with respect to the energy of the nominal cubic (Pm-3m) structure was calculated by using PBEsol functional. These polymorphous structures with multi-mode were obtained by force relaxation of the nudged, cubically shaped 4x4x4 supercell. The table also gives the Goldschmidt factor (t_{eff}) using Shannon ionic radii. The oxide perovskites listed have *p*-like VBM and *d*-like CBM, and the halide perovskites listed have *s*-like VBM and *p*-like CBM.

Energy lowering in cubic oxide perovskites			**Energy lowering cubic halide perovskites**		
(p, d*) ABO_3	t_{eff}	ΔE_M (meV/f.u.)	(s, p*) ABX_3	t_{eff}	ΔE_M (meV/f.u.)
$CaTiO_3$	0.97	-360	$CsSnI_3$	0.85	-38
$SrTiO_3$	1.00	-12	$CsPbI_3$	0.85	-69
$BaTiO_3$	1.06	-7	$KPbI_3$	0.80	-280
$SrZrO_3$	0.95	-21	$RbPbI_3$	0.82	-180
$PbZrO_3$	0.96	-44	$RbGeI_3$	0.95	-45
$PbTiO_3$	1.02	-6	$CsGeBr_3$	1.01	-40
$SnTaO_3$	0.98	-41	$CsGeI_3$	0.98	-30
/	/	/	$CsSnBr_3$	0.86	-10
/	/	/	$CsPbF_3$	0.91	-50
/	/	/	$CsPbBr_3$	0.82	-65

Table II also gives results for cubic ABO_3 oxide having a p-like valence band and d-like conduction band band-edge states, as well as halide perovskites ABX_3, showing significant energy lowering due to multi-mode within supercells, such as $SrZrO_3$, $PbZrO_3$, $CsGeBr_3$ and $CsPbBr_3$. We anticipate that the multi-mode can exist in other cubic perovskites with different band-edge states, such as $LaVO_3$ with (d, d*) states.[32] In the following sections, we mainly discuss the DOWPs and the corresponding effect on band gap by taking $ATiO_3$ (A^+ = Ca, Sr, Ba) and $CsBI_3$ (B^{2+} = Pb, Sn) as examples."

The multi-mode can lower the energy more than the single-mode because of a few reasons. First, instead of having a single mode with a large, uniform tilting angle and/or displacement throughout the lattice, it is sometimes energetically advantageous to have a few modes covering *a range* of tilting angles or displacements. Given the similar energy lowering for a single-mode with a large tilting angle and a few modes with small tilting angles, we anticipate that modes such as $a^-a^-a^-$, $a^0a^0b^-$ and $a^0b^-b^-$ modes in $SrTiO_3$, $a^0a^0b^-$ and $a^0a^0b^+$ modes in $CsPbI_3$, $a^-a^-a^-$, $a^0b^-b^-$, and $a^-a^-a^+$ modes in $CaTiO_3$ would coexist. This would lead to a mixture of different tilting modes with energy lowering. Indeed, as depicted in Fig. 2, the mixture mode $(a^0a^0b^1)_1^2(a^0a^0b^+)_2^3(a^0a^0b^-)_3^4$ in 4×4×4 supercell of the cubic $SrTiO_3$ has slightly lower energy (from -12 to -13 meV/f.u.) than the 2×2×2 supercell with the single $a^-b^-c^-$ mode.

Second, a larger supercell can enable relaxation modes absent in a smaller cell that has restricted single-mode. Again, $SrTiO_3$ supercell has multi-mode $(a^0a^0b^1)_1^2(a^0a^0b^+)_2^3(a^0a^0b^-)_3^4$ not allowed in 2×2×2 cell (Fig. 2). The x, y, z tilting angles in the 4×4×4 supercell are (3.5°, 5.9°, 4.9°), close to the values in relaxed 2×2×2 supercell with $a^-b^-c^-$ single-mode (Fig. 2).

C. Distribution of multi-mode tilting and displacements in polymorphous structures

Figure 3 analyzes the multi-mode statistics in polymorphous oxide perovskites $BaTiO_3$, $SrTiO_3$, and $CaTiO_3$. And Fig. 4 provides equivalent results for polymorphous structures of halide perovskites $CsPbI_3$ and $CsSnI_3$. Here, we focus on the B-site off-center displacements and the octahedral tilting angles with respect to <100>, <010> and <001> vectors, revealing distributed distortions of local motifs. In Fig. 3 and Fig. 4, the depicted distributions of octahedral tilting are different from the illustration shown in ref [28], which only shows the distribution of all tilting angles without differentiating the distribution along each direction. Here, by showing the corresponding distributed octahedral tilting angle with respect to <100>, <010>, and <001> vectors (defined as x, y and z directions), it can be seen if the DOWPs are single-mode or multi-mode. The results can be summarized as follows:

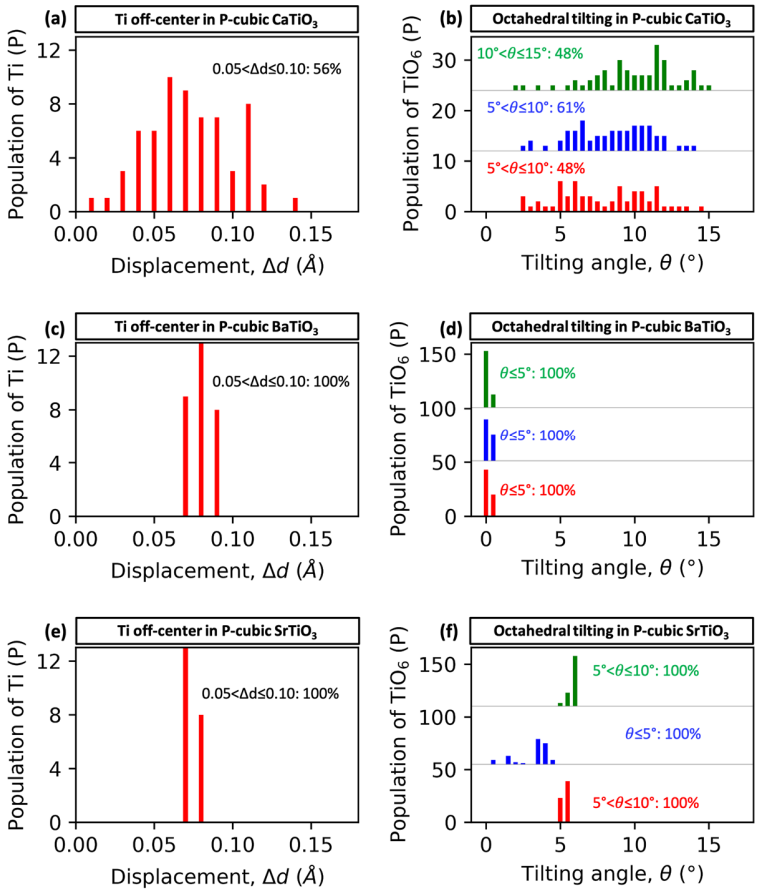

Figure 3. Statistical distributions of intrinsic multi-mode DOWPs in oxide perovskites: Shown are the number of Ti atoms with Ti off-center of different amplitudes (a, c, e) and octahedra with varying angles of tilting (b, d, f) with respect to Cartesian axes x (red bars), y (blue bars), and z (green bars) in 4×4×4 polymorphous cubic (P-cubic) $CaTiO_3$, $BaTiO_3$ and $SrTiO_3$ supercells. To zoom in on the distributed Ti, the y axis is not shown beyond y>15.

(i) *$CaTiO_3$ (Fig. 3a and 3b)*: The Ti displacements and octahedral tilting angles are distributed over relatively large ranges, though the major Ti displacements and octahedral tilting angles occur at 0.05 Å and ~11°, respectively. These Ti displacements and octahedral tilting distributions indicate the multi-mode in the polymorphous network.

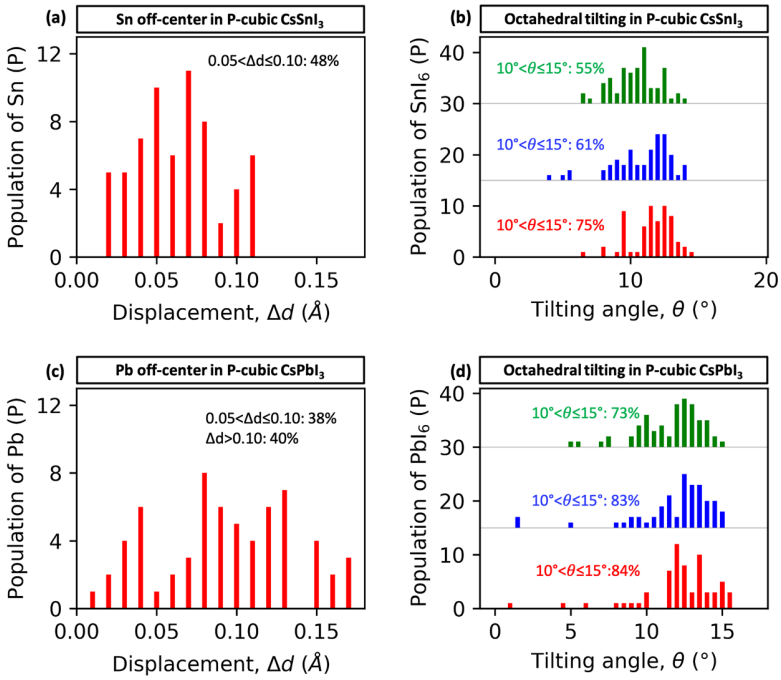

Figure 4. Statistical distribution of intrinsic multi-mode DOWPs in halide perovskites: Shown are the number of Sn/Pb atoms with Sn/Pb off-center of different amplitudes (a, c) and octahedra with varying angles of tilting (b, d) with respect to Cartesian axes x (red bars), y (blue bars), and z (green bars) in 4×4×4 polymorphous cubic (P-cubic) $CsSnI_3$ and $CsPbI_3$ supercells.

(ii) *$BaTiO_3$ (Fig. 3c and 3d)*: Ti displacements are mostly along {111} directions (close to the values of Ti displacements in the low-temperature orthorhombic structure[72]). Furthermore, there is negligible octahedral tilting, indicating a single ferroelectric static DOWPs mode (Fig. 2). Indeed, experimental PDF[73] suggests that this locally rhombohedral-like structure with Ti ferroelectric along {111} direction exists in paraelectric cubic $BaTiO_3$.

(iii) *$SrTiO_3$ (Fig. 3e and 3f)*: The Ti displacements and the octahedral tilting angles are distributed over narrow ranges (Ti displacements up to ~0.07 Å, tingle angle in a range of 0-6° along x, y, z axes). Note that the Sr atoms also slightly displace (up to 0.04 Å) from the perfect Wycoff position within a narrow range (Table I).

(iv) *$CsSnI_3$ and $CsPbI_3$ (Fig. 4):* The Sn or Pb displacements and octahedral tilting angles are distributed over a wide range (up to ~0.2 Å). Note that the B-site displacements and octahedral tilting angles in cubic $CsPbI_3$ are relatively larger than those in cubic $CsSnI_3$.

In short, there is a *distribution of local motifs* (here, B displacements and octahedral tilting angles) in cubic oxide and halide perovskites, forming a polymorphous network. And the smaller Goldschmidt factor (<1.0) implies larger octahedral tilting in a cubic structure, such as $CaTiO_3$.

D. Comparison of the multi-mode in polymorphous cubic $SrTiO_3$ with experimental pair distribution function probe

To examine whether the displacement pattern resulting from multi-mode relaxation is physically reasonable, we compare in Fig. 5 the calculated XRD diffraction and pair distribution function (PDF) obtained from the polymorphous cubic $SrTiO_3$ with the experimental PDF measured[74] at 225 K (calculations details in Supplementary section A). The width of the calculated XRD peaks conceal information on the statistic distribution of atom-atom bond lengths and short-range order. This information, not addressed in the present paper, awaits to be mined in the form of SRO parameters and pair distribution function (PDF) data as reported in ref [28]. The PDF is a local probe that reflects the distribution of atom-atom distances, thus a good way to determine the local atomic configurations and distortions within the system. As already noted, fitting the diffraction data in the Rietveld process to a single formula cubic (Pm-3m) cell[75] can miss the existence of intrinsic DOWPs that evidently lead to energy lowering (Fig. 1) when it is allowed to occur. We see in Fig. 5 that the DFT predicted PDF for oxide $SrTiO_3$ shows good agreement to the experiment. There are excellent agreements for halide perovskites between the calculated PDF from T=0 DFT and the measured PDF at finite moderate temperatures[76] such as $MAPbI_3$, etc.[28] provides additional evidence to the reasonableness of the DOWPs structures deduced from DFT. We note, however, that the tilting in $SrTiO_3$ is relatively small, as suggested by the tolerance factor being close to 1, so the dependence of PDF on the DOWPs is not as critical as in halide perovskites[28] or FeSe.[27]

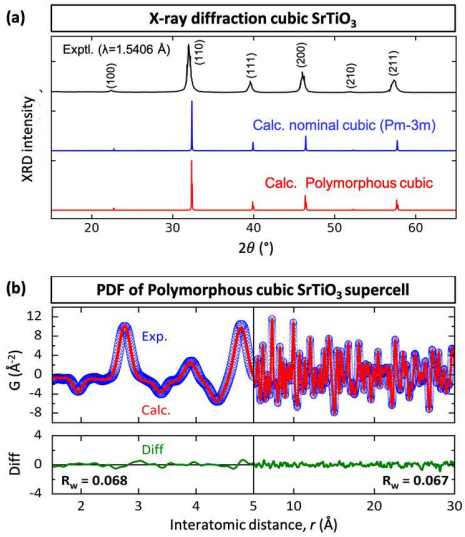

Figure 5. (a) Comparison of X-ray diffraction patterns among experimentally measured[77] $SrTiO_3$ single crystal (black line), simulated X-ray diffraction based on the calculated nominal cubic $SrTiO_3$ (blue line) and polymorphous 4x4x4 supercell with multi-mode DOWPs by using SCAN functional. The XRD peaks in the polymorphous network are slightly broadened relative to the monomorphous structure due to the absence of a strong correlation between the local motifs. (b) Comparison between experimentally measured[74] pair distribution function (PDF) of cubic $SrTiO_3$ at 225 K (empty blue circles) and DFT calculated PDF at T=0 (red lines) based on polymorphous 4x4x4 supercell optimized by SCAN functional. The overall R-factors are given for interatomic distance 0-5 Å (left) and 5-30 Å (right), revealing the derivation of the predicted PDF from the experimental measured PDF.

V. Effects of Intrinsic static single- and multi-mode DOWPs on band gaps

A. Effect of single-mode on band gap energy: turnover from blueshift at small deformations to redshift at large deformations

Using the structures with different single-mode (viz. Fig. 2) within frozen-in amplitudes in cubic 2x2x2 supercells, we have calculated non-perturbatively the corresponding band structure. Here, we deviate from the traditional perturbative treatment where electron-phonon interactions are summed explicitly (often with specific truncations). Figures 7 and 8 show for a few compounds, the band gap shifts due to specific deformation modes as a function of the amplitudes of distortion. Figure 6(a-c) shows that *the octahedral rotation in oxide perovskites leads to redshift when the tilting angle is larger than ~8°*. In contrast, smaller rotation angles and other modes (off-center, Jahn-Teller) lead to band gap *blueshift.* On

the other hand, for the *halide* perovskites (Figs. 8a and 8b), octahedral rotation between 0-15° always leads to band gap blueshift relative to the nominal cubic (Pm-3m) structure. For instance, for cubic $SrTiO_3$, the 15°-rotation angle for $a^0b^+b^+$ mode leads to a DFT gap of 1.57 eV (Fig. 6f), presenting 0.13 eV blueshift relative to the untitled, ideal structure. The $a^0b^+b^+$ single-mode in cubic $CaTiO_3$ with 15°-rotation angle leads to a DFT band gap of 0.93 eV (Fig. 6e), indicating a 0.75 eV redshift compared to the undistorted cubic (Pm-3m) structure. Table I provides a succinct summary. These trends are explained next.

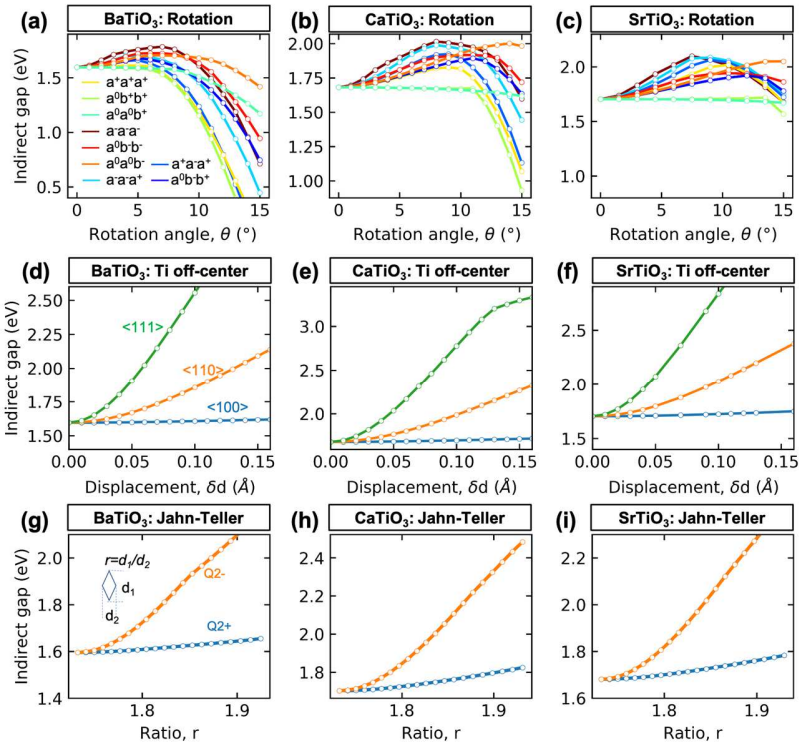

Figure 6. Cubic oxide perovskites: DFT Band gap changes as function of different single-mode with frozen-in amplitudes in cubic 2x2x2 supercells of $BaTiO_3$, $CaTiO_3$, $SrTiO_3$: (a-c) illustrated the gap shift by octahedral rotation mode, whereas (d-f) illustrate the gap shift by B-site off-center displacement along <100>, <110> and <111> directions. Panels (g-i) illustrate the effect of Jahn-Teller modes on the band gaps. Breathing modes and lattice expansion modes are also described in Supplementary Figure S-3. The Glazer notation for the off-center displacements, rotation, and the Jahn-Teller modes are depicted in inserts (a), (d), and (g), respectively.

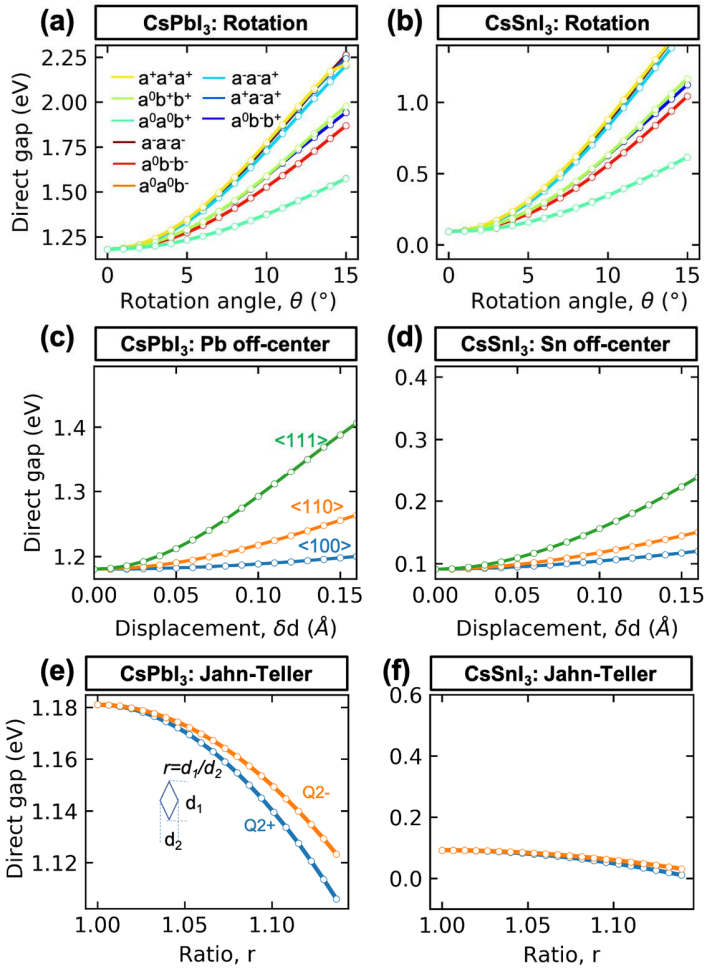

Figure 7. Cubic halide perovskites: DFT band gap changes as the function of different single-mode with frozen-in amplitudes in cubic 2x2x2 supercells of $CsPbI_3$ and $CsSnI_3$: (a, b) illustrate the effect of octahedral rotation modes on the band gap, (c, d) depict the band gap shift due to B site off-center along <100>, <110> and <111> directions, whereas (e, f) show the effect of Jahn-Teller modes on the band gaps of cubic $CsPbI_3$, $CsSnI_3$. Breathing modes and lattice expansion modes are illustrated in Supplementary Fig. S-4)

B. Blueshifts of the Indirect gap and redshift of the direct gap in cubic oxide $CaTiO_3$ as results of single-mode octahedral rotation

To understand the aforementioned band gap blue or red shift in oxide and halide perovskites due to the intrinsic DOWPs, we take cubic $CaTiO_3$ and $CsPbI_3$ as examples. Figure 8 shows the effective band structures (EBS)[78] and the energy diagram before and after octahedral rotation for the most energetically favorable frozen single Glazer mode. The EBS showed in Fig. 8a and 8b are unfolded band

structures transforming rigorously the band structure of large real space supercell to the Brillouin Zone appropriate to the primitive real space cell (details in Supplementary section A). As Fig. 8a illustrates, the octahedral rotation angle of $a^-a^-a^-$ mode at 5° in $CaTiO_3$ leads to an *increase* in the indirect band gap at *R*-Γ and a *decrease* in the direct band gap at Γ-Γ with respect to values in the untilted structure. These shifts reveal a transition from the indirect band gap in the untilted structure to a nearly degenerate direct-indirect band gap. For the cubic halide $CsPbI_3$, the rotation angle of $a^0a^0b^-$ mode at 5° results in an increase in the direct band gap at R-R with respect to undeformed structure.

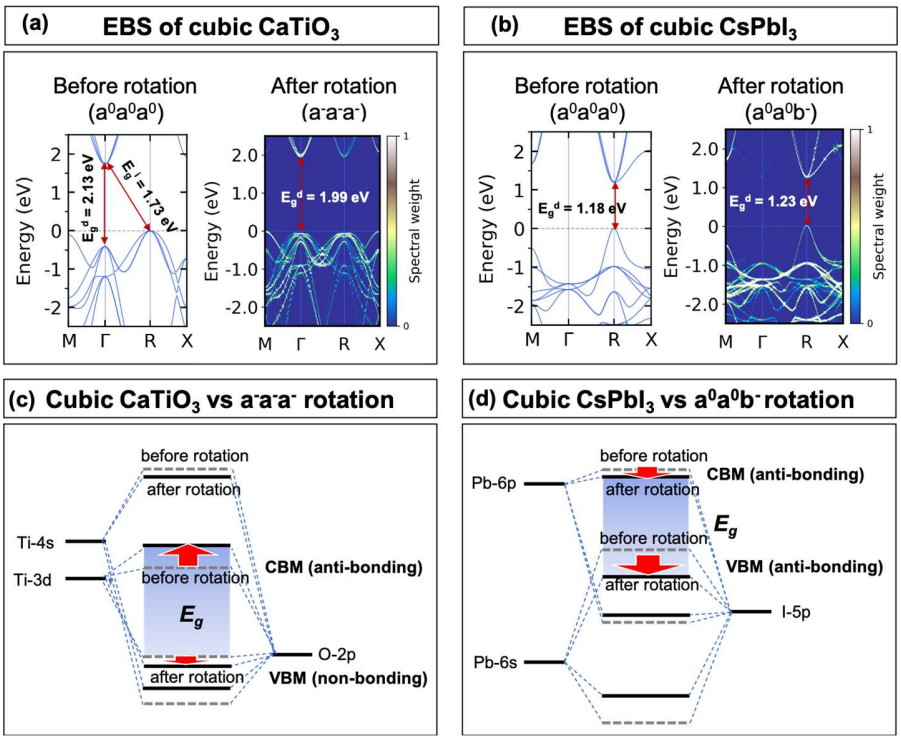

Figure 8. (a, b) the unfolded effective band structure (EBS) from 2x2x2 supercell to primitive cell (1fu/cell) of (c) cubic $CaTiO_3$ with $a^-a^-a^-$ single-mode energy lowering rotation mode and (d) cubic $CsPbI_3$ with $a^0a^0b^-$ energy lowering rotation mode. The amplitude of rotation angle in both (a) and (b) is frozen at 5°. The calculated indirect band gap (E_g^i) and direct band gap (E_g^d) are depicted in (a, b). The horizontal dash lines at zero in (c, d) band structures refer to the DFT calculated highest occupied level. (c, d) Energy level diagrams for $CaTiO_3$ and $CsPbI_3$ before and after octahedral rotation.

Figure 8c and 8d show the energy level diagrams for cubic $CaTiO_3$ and $CsPbI_3$ (referenced to the core-level of Ti-1*s* and Pb-1*s*) before and after octahedral rotation, which explains the above-noted DFT results. From Fig. 8c, we see that for the *cubic oxide CaTiO₃,* the VBM is a non-bonding state (O-*2p*), and the CBM

is an anti-bonding state (majority Ti-3*d*), whereas, for the cubic halide *$CsPbI_3$*, both VBM and CBM are anti-bonding states (Pb-*6s* – I-5*p* at VBM and Pb-*6p* – I-*5p* at CBM as illustrated in Fig. 8d). We find that the octahedral rotation in $CaTiO_3$ leads to enhanced interaction between Ti-3*d* and O-2*p* states, enlarging the corresponding splitting between bonding states inside the valence bands anti-bonding states at CBM. This splitting results in the *upshift* of the CBM in distorted $CaTiO_3$. At the same time, the VBM at the R point shifts to slightly deeper energies (due to the weakened repulsion of Ti-4*s* and O-2*p* bonding state), and the VBM at the Γ point upshifts (due to the enhanced repulsion between Ti-3*p* and O-2*p* non-bonding state at Γ point). Therefore, in cubic oxide $CaTiO_3$, *the R-Γ indirect gap blueshifts and Γ-Γ direct band gap redshifts* as a result of octahedral rotation. While the octahedral rotation in the cubic halide enlengthens Pb-I bond length hence weakens the Pb-I coupling. The weakened coupling results in a downshift of VBM and CBM energy levels. However, VBM downshifts more than CBM because VBM is more sensitive to the enlengthened bond length due to inner-shell Pb-6s states contributed to the VBM. *This leads to the R-R band gap blueshift in cubic halide $CsPbI_3$.*[79,80] The same mechanism persists in a polymorphous network with multi-mode distortions.

C. Emergence of a direct band gap component in $CaTiO_3$ and $SrTiO_3$ due to single-mode octahedra rotation

We have seen that in cubic oxide $CaTiO_3$, there is a transition from indirect to nearly degenerated indirect and direct band gap due to the octahedral rotation for $a^-a^-a^-$ single Glazer mode (Fig. 8a). Considering the unfolded band structure (Fig. 9a), we also find that other octahedral rotation modes, e.g., $a^0b^-b^-$, $a^+a^-a^+$, and $a^-a^-a^+$, in cubic $CaTiO_3$ lead to such indirect-to-direct band gap transition. Consequently, as can be seen from Fig. 8a and Fig. 9a, besides the already existing minimal R-Γ indirect gap, intrinsic DOWPs lead to minimal Γ-Γ direct band gap component as a secondary valley. Note that such a direct-in-momentum gap component is not a consequence of the folding mechanism in the supercell, because it survives in the EBS. A similar phenomenon is seen in cubic $SrTiO_3$.

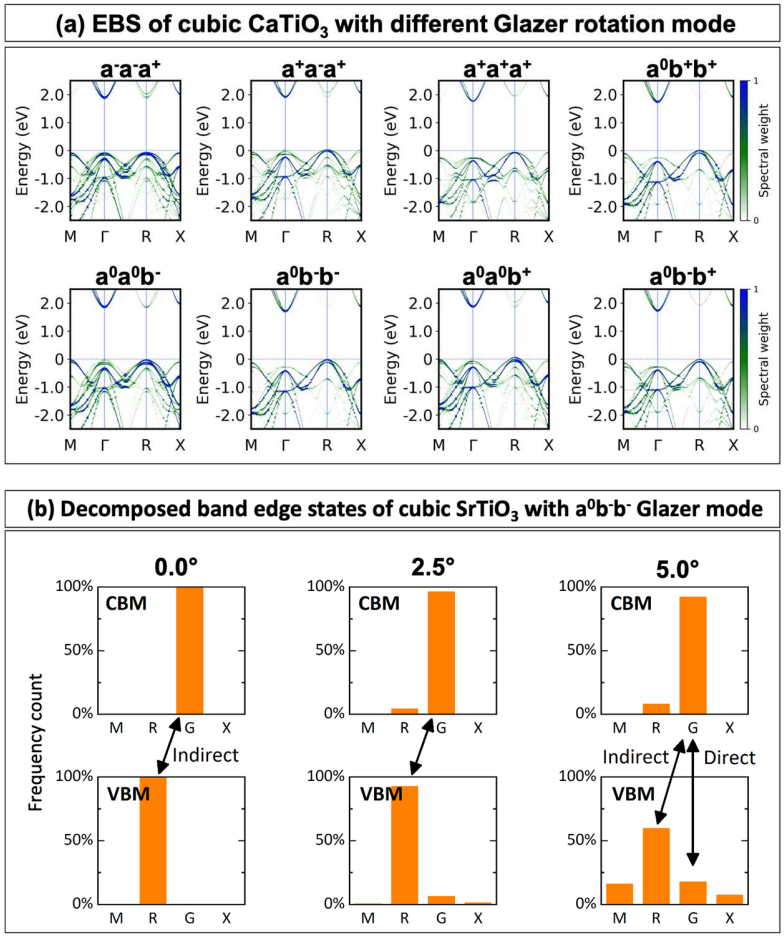

Figure 9. The effective band structure (EBS) of (a) $CaTiO_3$ in 2×2×2 supercell with frozen in single Glazer mode with frozen-in amplitudes of rotation angle 5°. $CaTiO_3$ has an indirect-to-direct band gap transition for the $a^-a^-a^+$ mode, while other Glazer modes have an indirect band gap from the VBM at the R point to the CBM at the Γ point. The horizon dash lines at zero in (c, d) band structures refer to the DFT calculated highest occupied level. (b) Direct-indirect gap transition in cubic $SrTiO_3$ as rotation angle increases. The VBM of cubic $SrTiO_3$ has more and more Γ components as rotation angle increases, meaning a larger and larger direct gap component.

To analyze the relationship between the direct gap component and the rotation DOWPs, Fig. 9b shows several cubic $SrTiO_3$ with frozen-in $a^0b^-b^-$ mode with a rotation angle of 0°, 2.5°, and 5°. The increase in rotation amplitude causes the VBM spectral intensity at Γ to increase, but VBM spectral intensity at R diminishes. These trends signal the buildup of a significant direct band gap component in cubic $SrTiO_3$ due to tilting DOWPs.

C. Effects of single-mode and multi-mode static non-thermal deformations on band gaps

Figure 10 summarizes for several cubic ABX_3 compounds (i) the minimal band gap from monomorphous (Pm-3m) cell (shown in blue), (ii) the gap resulting from allowing single-mode DOWPs that leads to the largest absolute energy lowering (shown in green), and (iii) the band gap due to multi-mode in the polymorphous network (in red). The single-mode in cubic $CaTiO_3$, $BaTiO_3$, $CsSnI_3$, and $CsPbI_3$ are $a^-a^-a^-$ modes, Ti off-center along <111> direction, $a^0a^0b^-$ and $a^0a^0b^-$ modes, respectively. As shown in Fig. 10, the cubic (Pm-3m) structures without symmetry breaking have the smallest band gaps. The blueshift of these band gap values due to single-mode are in the range of 0.05 eV for $BaTiO_3$ to 0.39 eV for $CaTiO_3$ with respect to their corresponding cubic (Pm-3m) structure without symmetry breaking. The cubic structures with multi-mode in polymorphous network show much larger blueshift values from 0.11 eV for $BaTiO_3$ to 0.55 eV for $CsSnI_3$. Local symmetry breaking, either single-mode or multi-mode, can lead to significant band gap blueshift.

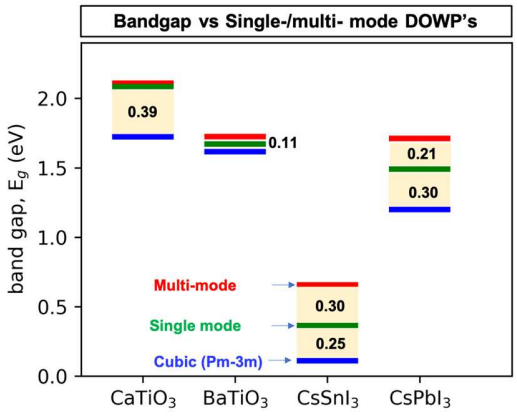

Figure 10. Minimal band gap E_g for (i) cubic Pm-3m (blue line) structure without distortion, (ii) the cubic structure with frozen in single-mode that results in the lowest energy lowering (green line), and (iii) multi-mode in the polymorphous network (red bar) of $CaTiO_3$, $BaTiO_3$, $CsSnI_3$, and $CsPbI_3$. The shaded regions highlight the band gap shift. The gap in the cubic (Pm-3m) structures refers to the indirect transition for oxide perovskites (R-Γ) to the (R-R) direct band gap for halide perovskites.

VI. Effect of Temperature-induced distortion in Molecular dynamics on band gaps

A. DFT Molecular Dynamics: Temperature-enhanced deformations in $CaTiO_3$ and $SrTiO_3$

The free energy of the vibrating lattice $F=U_0 - TS$ at finite temperature can be studied using MD simulations. As the temperature increases, the free energy decreases due to the $-TS$ term, which stabilizes the local distortion at finite temperature. In *ab initio* MD (AIMD) methodology, the finite-temperature dynamical trajectories are generated using forces obtained directly from electronic structure calculations. Therefore, phonon-phonon interactions are taken into account as the response of the electronic structure to deformations (represented in textbooks by the electron-phonon interactions). For several different temperatures, we extracted for each temperature N snapshots (N=2000 for $CaTiO_3$ and N=2471 for $SrTiO_3$) from the trajectory between 1ps – 2ps in AIMD calculations for cubic $CaTiO_3$ in a 4×4×4 supercell and cubic $SrTiO_3$ in a 5×5×5 supercell (from ref [54]). Note that in using a 5x5x5 supercell, the AIMD simulation of Ref 47 will not account for non-thermal octahedral tilting symmetry breaking, as illustrated in Fig. 1 but can allow for Sr and Ti off-center displacements. In contrast, the non-zero tilting angles seen in AIMD simulations might originate from the thermal motions of oxygen atoms. Thus, the restriction to 5x5x5 supercell permits thermal but excluded non-thermal octahedral tilting, whereas 4x4x4 cell allows both.

Since the distortions apparent from MD are rather complex and difficult to identify as specific, pure symmetry modes, we performed instead for each snapshot a statistical analysis of effective local octahedral tilting angles with respect to x, y, and z axes of the cubic cell as shown in Fig. 3 and Fig. 4. A similar analysis was done for Ti displacement with respect to the center of octahedra. The population (P) of tilted octahedra with specific tilting angle, Ti displacement, were depicted in Fig. 11.

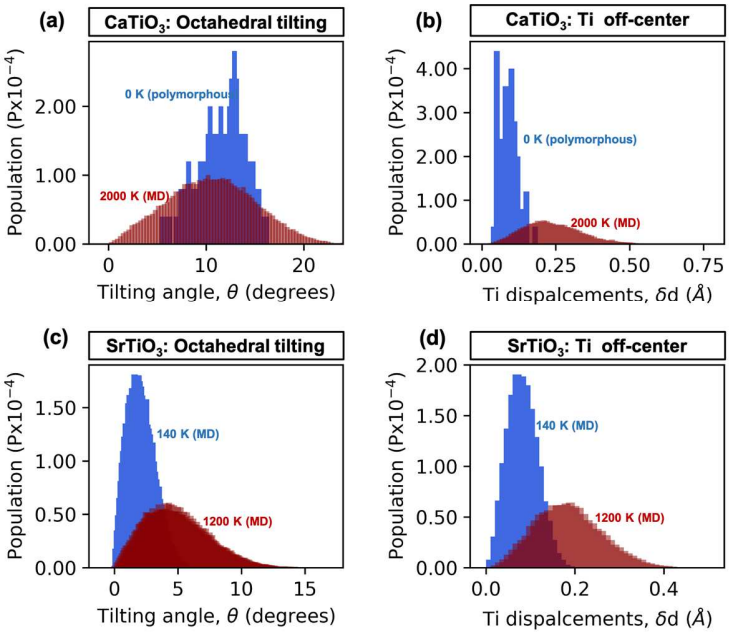

Figure 11. The distribution of populations of local distortions obtained from N snapshots using DFT Molecular Dynamic simulation in NVT ensemble for cubic $CaTiO_3$ in a 4×4×4 supercell (a-d) at 2000 K (dark-red bars), using the PBEsol functional and Gamma-only k-grid, and for $SrTiO_3$ in a 5×5×5 supercell at 140 K from Ref [54] (blue bars) and 1200 K (dark-red bars) employing the PBE functional with Tkatchenko-Scheffler dispersion correction[81] (e-h). The local distortions are Octahedral tilting angle (a, c) and Ti off-center displacements (b, d). For comparison, the statistical populations multiplied by 2000 of local distortions in 4×4×4 supercell $CaTiO_3$ polymorphous network were also depicted (a-d, blue bars). The data of $SrTiO_3$ are extracted data from reference.[54]

Figure 11 shows the thermally induced octahedral tilting and B-site displacement for cubic $CaTiO_3$ and $SrTiO_3$ at different temperatures. Significantly, the main peaks in Fig. 11a and 11c show a *broadening of the octahedral tilting angles around non-zero tilting angle values* from low temperature to high temperatures in cubic $CaTiO_3$ and $SrTiO_3$, as well as the Ti displacements. Notably, the amplitudes of A sites (Sr and Ca) displacements are significantly enlarged at high temperatures compared to B-site displacements (Table I). For example, the major Sr displacements start ~0.03 Å at T=0 (polymorphous structure) to ~0.23 Å at 1400 K. The presence of snapshot averaged *non-zero* distortions at low temperatures represent the intrinsic DOWPs of Ti displacements. The thermal-induced octahedral tilting and Ti off-center displacements are enhanced as temperature increases. This is consistent with enlarged Li displacements (rather than diminished displacements) as temperature increase in paraelectric $LiNbO_3$.[39]

B. The effects on band gap shift due to thermal distortion in oxide perovskites

The enhanced thermal motions revealed by the MD simulations result in significant band gap changes. For instance, the averaged band gap (expressed as $\sum_{i=1}^{N} E_g(S_i)/N$ of individual configuration S_i along the thermodynamic equilibrium trajectory) for cubic $CaTiO_3$ and $SrTiO_3$ (Table I). The band gap redshift due to thermal motions at 2000 K in cubic $CaTiO_3$ is -1.15 eV with respect to polymorphous structure and -0.77 eV with respect to the nominal cubic structure. Similarly, in cubic $SrTiO_3$, the corresponding band gap redshifts are 0.72 eV and 0.49 eV, respectively, at 1400 K. Evidently, thermal motions in cubic $CaTiO_3$ and $SrTiO_3$ lead to significantly band gap red shift at high temperature (>T_c) with respect to band gap at T=0 (monomorphous structure).

Table I provides both a preview and a succinct summary of the main differences between the effects of static non-thermal vs. dynamic thermal displacements on band gaps:

For oxide perovskites: Different from nominal cubic $SrTiO_3$ and $CaTiO_3$ with *p*-like VBM and *d*-like CBM, the "correlated" Mott insulators having *d*-like VBM and *d*-like CBM (d, d*) in the nominal cubic structure are often high energy false metals because of the absence of DOWPs. This led the *d*-electron oxide literature to postulate the need for dynamic electron correlation for opening the gap.[32,82] Allowing the formation of polymorphous cubic structure lowers the energy and correctly becomes an insulator even for (d, d*) because of structural and electronic symmetry breaking by energy lowering, such as $LaTiO_3$, $LaVO_3$.[30,32] The reason is that the gap increases with tilting in the range of XX angles (see Fig. 6). Finally, at really high T cubic phases, we have larger amplitudes of DOWPs; for some of the Glazer modes, such high tilting exists in MD for oxides, and reverses the direction of gap changes from blueshifts at low amplitude to redshift at high amplitudes. Thus, at such temperatures system can convert to metal.
For halides perovskites: These are never (*d*, *d**) but rather (*s*, *p**) compounds, and as such, they have finite gaps even in the nominal cubic structure, albeit rather underestimated. Allowing for DOWPs lowers the internal energy and increases the band gaps; such polymorphous structures have relatively larger band gap values, sometimes comparable to those of the low-temperature low-symmetry structures. The reason is that at low tilting angles, the gap increases with tilting. At really high T, gaps continue to rise because tilting angles increase, and the band gap is always blue shifted.

VII. Conclusions

We offer a structural approximant to the cubic perovskites that replaces the nominally cubic (Pm-3m) anzats that restricts deformations. The polymorphous anzats are based on nudging the internal positions of a cubically shaped supercell that is initially made from replicas of the cubic (Pm-3m) monomorphous primitive cell. This results in the formation of local distortions that can be characterized as short-range order without long-range order". Such nudged cubic supercell excites multi-mode results in lower total energy and many local, static motifs even before the thermal effects set in. The local static DOWPs is an expression of the nature of chemical bonding in the compounds, projecting onto many symmetry-breaking modes such as A and B site off-center, octahedral tilting/rotation, breathing mode. The static DOWPs not only agree with local probe (such as PDF) observations in the experiment, but also show significant contribution to the changes of electronic structure. We can summarize the conclusions as follows:

(i) Comparison between Halide and Oxide perovskites. We learned that oxides and halides respond differently to static distortions. Cubic halide and oxide perovskites adopt different energy lowering symmetry-breaking modes. In cubic $CaTiO_3$ and $SrTiO_3$, such intrinsic DOWPs lead to a predicted yet not

reported Γ-Γ direct band gap component, as a secondary valley minimum to the well-known indirect R-Γ gap. In contrast, intrinsic DOWPs only enlarge the direct band gap blueshift. This might provide the possibility to tune the indirect-to-direct transition in oxide perovskites by controlling a specific mode. However, in cubic halide perovskites, intrinsic DOWPs do not lead to band-edge transformation but direct band gap blueshift. Besides, different from the flat valence band-edge states in oxide perovskites with DOWPs, the valence band-edge states of halide perovskites contributed by the lone pair states remain sharp, indicating the weak coupling between conductivity and distortion. This provides a good principle to design optoelectrical materials with excellent conductivity.

(ii) Comparison of static vs. dynamic thermal effect in the cubic phases: Thermal motion creates redshift in oxide perovskites and blue shift in halide perovskites, whereas the static local symmetry-breaking usually results in band gap blueshift in oxide and halide perovskites. The observed band-gap renormalization in cubic phase at high temperature is then the constructive (as in halide perovskite) or destructive (as in oxide perovskites) superposition of the DOWPs effect and thermal motion. Consequently, the real band-gap renormalization at finite temperature ($T > T_c$) is underestimated for oxide perovskites and overestimated for halide perovskites with respect to the nominal cubic structure (Pm-3m).

This study clarifies the role of intrinsic symmetry breaking on the properties of cubic perovskites, separating them from the traditional thermal effects. Static DOWPs rather than thermal motions can break the centrosymmetric symmetry (Pm-3m), making materials acquire unique functionality in cubic phase such as strong Rashba effect, Raman effect, piezoelectric effect or second harmonic generation, etc.

Acknowledgements:

The work at the University of Colorado at Boulder was supported by the DMREF program of the U.S. National Science Foundation through Grant No. DMREF-1921949. Work on the calculations of optimizations of supercells was supported by the U.S. Department of Energy, Office of Science, Basic Energy Sciences, Materials Sciences and Engineering Division, under Grant No. DE-SC0010467 to the University of Colorado. The calculations of effective band structures of supercells and phonons were computed on XSEDE supercomputers. We thank Dr. C. M. Culbertson, who kindly shared experimental PDF data of cubic $SrTiO_3$, and thank Dr. M. Zacharias, who kindly shared the trajectory files of MD simulations for cubic $SrTiO_3$.

References:

[1] M. Yashima, M. Tanaka, J Appl Cryst 37 (2004) 786–790.
[2] S. Aoyagi, Y. Kuroiwa, A. Sawada, I. Yamashita, T. Atake, J. Phys. Soc. Jpn. 71 (2002) 1218–1221.
[3] Z. Salman, R.F. Kiefl, K.H. Chow, M.D. Hossain, T.A. Keeler, S.R. Kreitzman, C.D.P. Levy, R.I. Miller, T.J. Parolin, M.R. Pearson, H. Saadaoui, J.D. Schultz, M. Smadella, D. Wang, W.A. MacFarlane, Phys. Rev. Lett. 96 (2006) 147601.
[4] B. Wang, N. Novendra, A. Navrotsky, J. Am. Chem. Soc. 141 (2019) 14501–14504.
[5] K. Yamada, S. Funabiki, H. Horimoto, T. Matsui, T. Okuda, S. Ichiba, Chem. Lett. 20 (1991) 801–804.
[6] H.M. Rietveld, J Appl Cryst 2 (1969) 65–71.
[7] (n.d.).
[8] D. Zagorac, H. Müller, S. Ruehl, J. Zagorac, S. Rehme, J Appl Cryst 52 (2019) 918–925.
[9] M.J. Mehl, D. Hicks, C. Toher, O. Levy, R.M. Hanson, G. Hart, S. Curtarolo, Computational Materials Science 136 (2017) S1–S828.
[10] A. Jain, S.P. Ong, G. Hautier, W. Chen, W.D. Richards, S. Dacek, S. Cholia, D. Gunter, D. Skinner, G. Ceder, K.A. Persson, APL Materials 1 (2013) 011002.
[11] S. Tariq, A. Ahmed, S. Saad, S. Tariq, AIP Advances 5 (2015) 077111.
[12] S. Saha, T.P. Sinha, A. Mookerjee, Eur. Phys. J. B 18 (2000) 207–214.
[13] S. Saha, T.P. Sinha, A. Mookerjee, Phys. Rev. B 62 (2000) 8828–8834.
[14] R.A. Evarestov, V.P. Smirnov, D.E. Usvyat, Solid State Communications 127 (2003) 423–426.
[15] A.R. Benrekia, N. Benkhettou, A. Nassour, M. Driz, M. Sahnoun, S. Lebègue, Physica B: Condensed Matter 407 (2012) 2632–2636.
[16] R. Ahuja, O. Eriksson, B. Johansson, Journal of Applied Physics 90 (2001) 1854–1859.
[17] M. Afsari, A. Boochani, M. Hantezadeh, Optik 127 (2016) 11433–11443.
[18] S. McKechnie, J.M. Frost, D. Pashov, P. Azarhoosh, A. Walsh, M. van Schilfgaarde, Phys. Rev. B 98 (2018) 085108.
[19] S. Poncé, M. Schlipf, F. Giustino, ACS Energy Lett. 4 (2019) 456–463.
[20] S. Tinte, M.G. Stachiotti, M. Sepliarsky, R.L. Migoni, C.O. Rodriguez, J. Phys.: Condens. Matter 11 (1999) 9679–9690.
[21] K. Parlinski, Y. Kawazoe, Y. Waseda, J. Chem. Phys. 114 (2001) 2395–2400.
[22] J.-J. Zhou, O. Hellman, M. Bernardi, Phys. Rev. Lett. 121 (2018) 226603.
[23] A. Marronnier, G. Roma, S. Boyer-Richard, L. Pedesseau, J.-M. Jancu, van Bonnassieux, C. Katan, C.C. Stoumpos, M.G. Kanatzidis, J. Even, in: 2018 IEEE 7th World Conference on Photovoltaic Energy Conversion (WCPEC) (A Joint Conference of 45th IEEE PVSC, 28th PVSEC 34th EU PVSEC), 2018, pp. 1715–1717.
[24] A. Bano, P. Khare, N.K. Gaur, R. Chitra, S. Bhattacharya, N.K. Sahoo, AIP Conference Proceedings 1731 (2016) 090001.
[25] R.X. Yang, J.M. Skelton, E.L. da Silva, J.M. Frost, A. Walsh, J. Phys. Chem. Lett. 8 (2017) 4720–4726.
[26] R.X. Yang, J.M. Skelton, E.L. da Silva, J.M. Frost, A. Walsh, J. Chem. Phys. 152 (2020) 024703.
[27] Z. Wang, X.-G. Zhao, R. Koch, S.J.L. Billinge, A. Zunger, Phys. Rev. B 102 (2020) 235121.
[28] X.-G. Zhao, G.M. Dalpian, Z. Wang, A. Zunger, Phys. Rev. B 101 (2020) 155137.
[29] Z. Wang, O.I. Malyi, X. Zhao, A. Zunger, ArXiv:2006.10099 [Cond-Mat] (2020).
[30] J. Varignon, M. Bibes, A. Zunger, Phys. Rev. Research 1 (2019) 033131.
[31] O.I. Malyi, A. Zunger, Applied Physics Reviews 7 (2020) 041310.
[32] J. Varignon, M. Bibes, A. Zunger, Nat Commun 10 (2019) 1–11.
[33] Q. Zhang, T. Cagin, W.A. Goddard, PNAS 103 (2006) 14695–14700.
[34] B. Monserrat, D. Vanderbilt, ArXiv:1711.06274 [Cond-Mat] (2017).
[35] W. Prusseit-Elffroth, F. Schwabl, Appl. Phys. A 51 (1990) 361–368.
[36] J.H. Lee, K.M. Rabe, Phys. Rev. B 84 (2011) 104440.
[37] M.-C. Jung, K.-W. Lee, Phys. Rev. B 90 (2014) 045120.
[38] J. Wiktor, U. Rothlisberger, A. Pasquarello, J. Phys. Chem. Lett. 8 (2017) 5507–5512.
[39] S.R. Phillpot, V. Gopalan, Appl. Phys. Lett. 84 (2004) 1916–1918.
[40] K.A. Müller, Y. Luspin, J.L. Servoin, F. Gervais, J. Phyique Lett. 43 (1982) 537–542.
[41] E.A. Stern, Phys. Rev. Lett. 93 (2004) 037601.
[42] W.P. Mason, B.T. Matthias, Phys. Rev. 74 (1948) 1622–1636.
[43] M.E. Lines, A.M. Glass, Principles and Applications of Ferroelectrics and Related Materials, OUP Oxford, 2001.

[44] E.K.H. Salje, M.A. Carpenter, G.F. Nataf, G. Picht, K. Webber, J. Weerasinghe, S. Lisenkov, L. Bellaiche, Phys. Rev. B 87 (2013) 014106.
[45] A. Jain, S.P. Ong, G. Hautier, W. Chen, W.D. Richards, S. Dacek, S. Cholia, D. Gunter, D. Skinner, G. Ceder, K.A. Persson, APL Materials 1 (2013) 011002.
[46] R. Allmann, R. Hinek, Acta Cryst A 63 (2007) 412–417.
[47] H.T. Dang, A.J. Millis, C.A. Marianetti, Phys. Rev. B 89 (2014) 161113.
[48] K. Held, I.A. Nekrasov, N. Blümer, V.I. Anisimov, D. Vollhardt, Int. J. Mod. Phys. B 15 (2001) 2611–2625.
[49] A. Georges, G. Kotliar, W. Krauth, M.J. Rozenberg, Rev. Mod. Phys. 68 (1996) 13–125.
[50] L. Nordheim, Annalen Der Physik 401 (1931) 607–640.
[51] F. Yonezawa, K. Morigaki, Progress of Theoretical Physics Supplement 53 (1973) 1–76.
[52] A.M. Glazer, Acta Cryst B 28 (1972) 3384–3392.
[53] S. Ishiwata, M. Tokunaga, Y. Kaneko, D. Okuyama, Y. Tokunaga, S. Wakimoto, K. Kakurai, T. Arima, Y. Taguchi, Y. Tokura, Phys. Rev. B 84 (2011) 054427.
[54] M. Zacharias, M. Scheffler, C. Carbogno, Phys. Rev. B 102 (2020) 045126.
[55] O.I. Malyi, A. Zunger, Applied Physics Reviews 7 (2020) 041310.
[56] L. Granlund, S.J.L. Billinge, P.M. Duxbury, Acta Cryst A 71 (2015) 392–409.
[57] K. Sato, T. Miyanaga, S. Ikeda, D. Diop, Phys. Scr. 2005 (2005) 359.
[58] D.C. Arnold, K.S. Knight, G. Catalan, S.A.T. Redfern, J.F. Scott, P. Lightfoot, F.D. Morrison, Advanced Functional Materials 20 (2010) 2116–2123.
[59] J. Sun, A. Ruzsinszky, J.P. Perdew, Phys. Rev. Lett. 115 (2015) 036402.
[60] J.P. Perdew, A. Ruzsinszky, G.I. Csonka, O.A. Vydrov, G.E. Scuseria, L.A. Constantin, X. Zhou, K. Burke, Phys. Rev. Lett. 100 (2008) 136406.
[61] F.W. Lytle, Journal of Applied Physics 35 (1964) 2212–2215.
[62] A.M. Glazer, Acta Cryst B 28 (1972) 3384–3392.
[63] P.M. Woodward, Acta Cryst B 53 (1997) 32–43.
[64] D.H. Fabini, G. Laurita, J.S. Bechtel, C.C. Stoumpos, H.A. Evans, A.G. Kontos, Y.S. Raptis, P. Falaras, A. Van der Ven, M.G. Kanatzidis, R. Seshadri, J. Am. Chem. Soc. 138 (2016) 11820–11832.
[65] R.C. Remsing, M.L. Klein, APL Materials 8 (2020) 050902.
[66] B.B. Van Aken, T.T.M. Palstra, A. Filippetti, N.A. Spaldin, Nature Materials 3 (2004) 164–170.
[67] P.M. Woodward, Acta Cryst B 53 (1997) 44–66.
[68] J.M. Rondinelli, C.J. Fennie, Advanced Materials 24 (2012) 1961–1968.
[69] E.H. Smith, N.A. Benedek, C.J. Fennie, Inorg. Chem. 54 (2015) 8536–8543.
[70] P. Garcia-Fernandez, J.A. Aramburu, M.T. Barriuso, M. Moreno, J. Phys. Chem. Lett. 1 (2010) 647–651.
[71] A. Mercy, J. Bieder, J. Íñiguez, P. Ghosez, Nature Communications 8 (2017) 1677.
[72] G. Shirane, H. Danner, R. Pepinsky, Phys. Rev. 105 (1957) 856–860.
[73] M.S. Senn, D.A. Keen, T.C.A. Lucas, J.A. Hriljac, A.L. Goodwin, Phys. Rev. Lett. 116 (2016) 207602.
[74] C.M. Culbertson, A.T. Flak, M. Yatskin, P.H.-Y. Cheong, D.P. Cann, M.R. Dolgos, Scientific Reports 10 (2020) 1–10.
[75] A. Belsky, M. Hellenbrandt, V.L. Karen, P. Luksch, Acta Cryst B 58 (2002) 364–369.
[76] A.N. Beecher, O.E. Semonin, J.M. Skelton, J.M. Frost, M.W. Terban, H. Zhai, A. Alatas, J.S. Owen, A. Walsh, S.J.L. Billinge, ACS Energy Lett. 1 (2016) 880–887.
[77] X. Wei, G. Xu, Z. Ren, C. Xu, W. Weng, G. Shen, G. Han, Journal of the American Ceramic Society 93 (2010) 1297–1305.
[78] V. Popescu, A. Zunger, Phys. Rev. Lett. 104 (2010) 236403.
[79] G.M. Dalpian, X.-G. Zhao, L. Kazmerski, A. Zunger, Chem. Mater. 31 (2019) 2497–2506.
[80] Z. Xiao, D.B. Mitzi, Y. Yan, (n.d.).
[81] A. Tkatchenko, M. Scheffler, Phys. Rev. Lett. 102 (2009) 073005.
[82] M. De Raychaudhury, E. Pavarini, O.K. Andersen, Phys. Rev. Lett. 99 (2007) 126402.

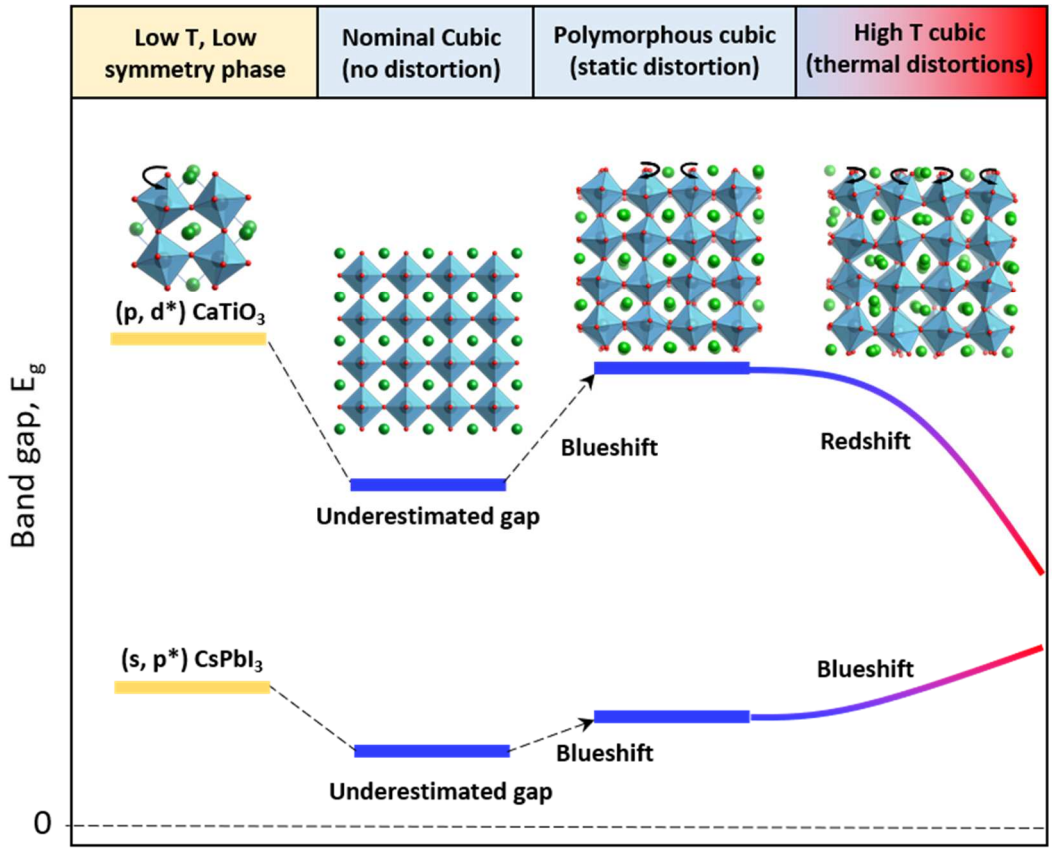
Low T, Low symmetry phase
Nominal Cubic (no distortion)
Polymorphous cubic (static distortion)
High T cubic (thermal distortions)
Band gap, E_g
(p, d*) $CaTiO_3$
Underestimated gap
Blueshift
Redshift
(s, p*) $CsPbI_3$
Underestimated gap
Blueshift
Blueshift
0